AGU PUBLICATIONS

Geophysical Research Letters

RESEARCH LETTER
10.1002/2015GL065701

Key Points:
- Grounding line of Totten Glacier is retreating, not as fast as West Antarctica
- Retreat pattern explained by the newly inferred bed geometry
- If ice thinning maintains, bed geometry conducive to further retreat

Supporting Information:
- Figures S1–S5, Table S1, and Text S1

Correspondence to:
X. Li,
xin.li@uci.edu

Citation:
Li, X., E. Rignot, M. Morlighem, J. Mouginot, and B. Scheuchl (2015), Grounding line retreat of Totten Glacier, East Antarctica, 1996 to 2013, *Geophys. Res. Lett.*, *42*, 8049–8056, doi:10.1002/2015GL065701.

Received 7 AUG 2015
Accepted 15 AUG 2015
Accepted article online 21 AUG 2015
Published online 9 OCT 2015

Grounding line retreat of Totten Glacier, East Antarctica, 1996 to 2013

Xin Li[1], Eric Rignot[1,2], Mathieu Morlighem[1], Jeremie Mouginot[1], and Bernd Scheuchl[1]

[1]Department of Earth System Science, University of California, Irvine, California, USA, [2]Jet Propulsion Laboratory, California Institute of Technology, Pasadena, California, USA

Abstract Totten Glacier, East Antarctica, a glacier that holds a 3.9 m sea level change equivalent, has thinned and lost mass for decades. We map its grounding line positions in 1996 and 2013 using differential radar interferometry (InSAR) data and develop precise, high-resolution topographies of its ice surface and ice draft using NASA Operation IceBridge data, InSAR data, and a mass conservation method. We detect a 1 to 3 km retreat of the grounding line in 17 years. The retreat is asymmetrical along a two-lobe pattern, where ice is only grounded a few 10 m above sea level, or ice plain, which may unground further with only modest amounts of ice thinning. The pattern of retreat indicates ice thinning of 12 m in 17 years or 0.7±0.1 m/yr at the grounding line on average. Sustained thinning will cause further grounding line retreat but may not be conducive to a marine instability.

1. Introduction

Totten Glacier (TG), the largest discharger of ice in East Antarctica [*Rignot*, 2006], drains a sector 537,900 km^2 in size, mostly grounded below sea level [*Young et al.*, 2011; *Wright et al.*, 2012] (Figure 1). TG holds an ice volume equivalent to 3.9 m global sea level rise, comparable to the West Antarctic Ice Sheet [*Fretwell et al.*, 2013; *Bamber et al.*, 2009]. Its mass flux into the ocean of 71 ± 3 Gt/yr in 2007–2008 was out of balance with its long-term (1979–2004) average mass input from snowfall of 67 ± 3 Gt/yr [*Rignot et al.*, 2013; *Lenaerts and van den Broeke*, 2012]; i.e., the glacier has been losing mass [*Rignot and Thomas*, 2002; *Rignot*, 2008]. The mass loss has been confirmed by Gravity Recovery and Climate Experiment time-variable gravity data [*Chen et al.*, 2009; *Velicogna et al.*, 2014]. Radar altimetry from the European Remote Sensing (ERS) 1 and 2, Envisat and CryoSat-2 satellites, and NASA's Ice, Cloud,and land Elevation Satellite laser altimetry mission indicate that the glacier is thinning at low elevation, close to its grounding line or junction with the ocean. The reported thinning rates increased from about 0.5 m/yr in the 1990s [*Shepherd and Wingham*, 2007; *Zwally et al.*, 2005] to about 1.5 m/yr in 2003–2009 [*Pritchard et al.*, 2009; *Horwath et al.*, 2012; *Flament and Rémy*, 2012] and may have decreased in recent years [*McMillan et al.*, 2014] (see Table S1 in the supporting information). A large share of the ice shelf thickness has not been changing at a significant level over the past two decades [*Paolo et al.*, 2015]. Yet the concentration of thinning in areas of fast flow remains indicative of a change in ice flow dynamics, not a change in surface mass balance.

Warm, salty, subsurface Modified Circumpolar Deep Water (MCDW) has been observed on the continental shelf in front of TG [*Bindoff et al.*, 2000; *Williams et al.*, 2011]. A recent study indicates the possibility of a pathway for MCDW intrusion beneath the shelf [*Greenbaum et al.*, 2015]. Totten ice shelf experiences high ice shelf melt rates compared to other ice shelves in East Antarctica [*Rignot et al.*, 2013; *Pritchard et al.*, 2012]. The ice shelf melt rates may be influenced by coastal polynya activity [*Khazendar et al.*, 2013; *Gwyther et al.*, 2014] or enhanced advection of MCDW in response to a strengthening of the westerlies [*Spence et al.*, 2014]. The potential for an ocean-driven thinning is of importance because TG is connected to the deep Vanderford Subglacial Trench to the west and the Aurora Subglacial Basin to the south [*Young et al.*, 2011], i.e., areas where the bed is deepening inland hence potentially conducive to marine ice sheet instability [*Weertman*, 1974; *Sun et al.*, 2014; *Greenbaum et al.*, 2015; *Pollard et al.*, 2015], similar to the Amundsen Sea sector of West Antarctica [*Rignot et al.*, 2014].

Here we present a study of the grounding line of TG using Differential Synthetic-Aperture Radar Interferometry (D-InSAR) data from 1996 and 2013. The data are complemented by new, high-resolution maps of the glacier surface elevation and of its ice draft using radar-derived ice thickness from NASA's Operation

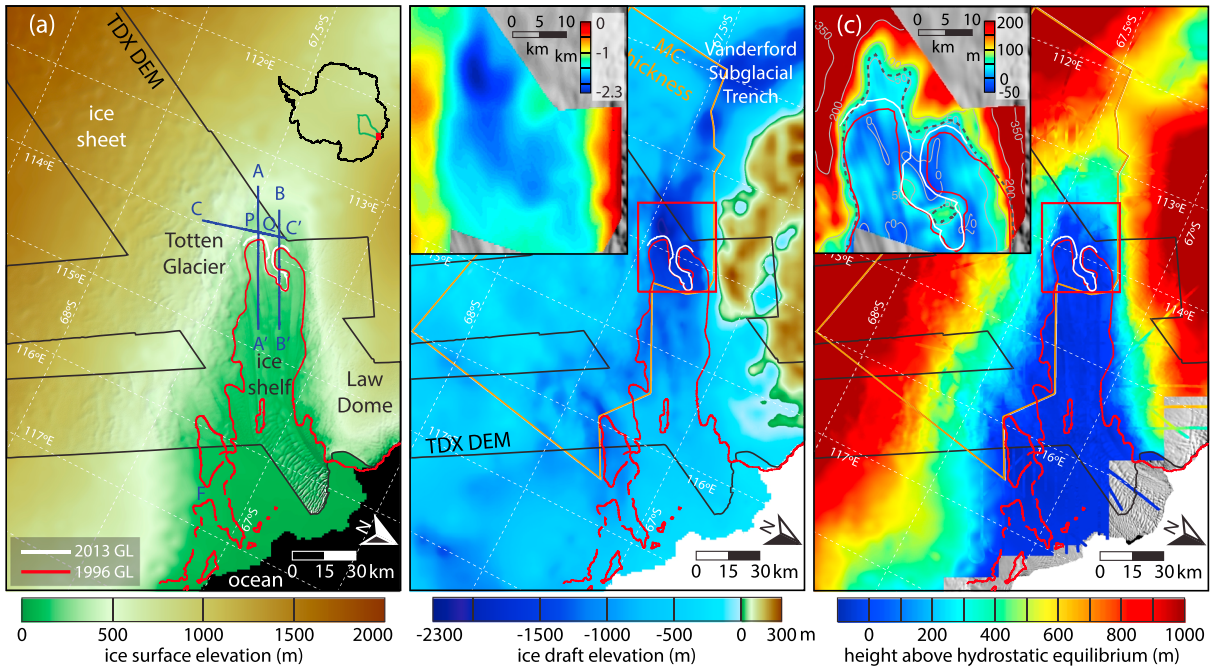

Figure 1. (a) Surface topography of Totten Glacier, East Antarctica, (b) ice draft topography, and (c) height above hydrostatic equilibrium. Black polygons denote the boundaries of TDX DEM mapping versus BEDMAP 2 [*Fretwell et al.*, 2013]. Orange polygons delineate the boundaries of the mass conservation (MC) domain. Red lines are OIB ground tracks discussed in Figure 3. Insets in Figures 1b and 1c are the ice draft elevation and the height above hydrostatic equilibrium, respectively, on a different color scale. Grounding line is solid white (2013), solid red (1996), and dotted black (projection for 10 m thinning, inset of Figure1c).

IceBridge (OIB) [*Blankenship et al.*, 2011, updated 2011, updated 2013], combined with InSAR-derived velocity and topography data. We compare the pattern of grounding line retreat in the 17 intervening years with the high-resolution glacier geometry to conclude on the evolution of the glacier and discuss its potential for future change.

2. Data and Methods

Ice Velocity. We map ice velocity by applying a speckle tracking technique on basin-scale Japanese Advanced Land Observation Satellite (ALOS) Phased Array type L-band Synthetic Aperture Radar (PALSAR) data (Figures S1 and S2). To fill in data gaps in *Rignot et al.* [2011b], we use additional ALOS PALSAR tracks from years 2006, 2007, and 2010 and adopt the stacking scheme from *Mouginot et al.* [2012]. The resulting mosaic of ice velocity is calibrated over the entire glacier drainage basin using stagnant areas (e.g., Law Dome), and the ice divides following *Mouginot et al.* [2012]. The final velocity map is posted at 600 m spacing. At the grounding line, the glacier flow speed is 850 m/yr at the center and 500 m/yr along the broad side that extends to the east of the main trunk (Figure S2). The glacier forms an ice shelf about 5903 km^2 in size with a frontal flow speed of 1700 m/yr and a calf-ice production of 28 $\pm$ 2 Gt/yr [*Rignot et al.*, 2013].

Ice Thickness. Ice thickness was measured by the NASA OIB mission ranging from the years 2009 to 2012 [*Blankenship et al.*, 2011, updated 2011, updated 2013]. At the grounding line, the glacier is 2000 to 2300 m thick. The track spacing of the OIB data is 4 km near the grounding line, which is not sufficient to resolve important details about the bed geometry. We derive a new map of ice thickness using a mass conservation (MC) method [*Morlighem et al.*, 2011] that combines the NASA OIB data with the high-resolution (600 m) ice velocity mosaic described earlier. The calculation includes surface mass balance from the Regional Atmospheric and Climate model (RACMO2) [*Lenaerts and van den Broeke*, 2012] and ice shelf melt rates from [*Rignot et al.*, 2013]. The MC ice thickness map has a 600 m spacing and a vertical precision of 60 m (Figure S3). This map is a major improvement compared to earlier maps derived from the kriging of OIB ice thickness data at 5 km spacing (e.g., BEDMAP 2 [*Fretwell et al.*, 2013]).

Ice Surface and Bottom Topography. To convert ice thickness into ice draft, we employ a surface Digital Elevation Model (DEM) (Figure 1a) derived from the German TanDEM-X (TDX) satellites (Table 1). InSAR pairs

Table 1. InSAR Satellite Data Used to Map the Grounding Line of Totten Glacier, East Antarctica: Sensor Name, Radar Wavelength λ in Centimeters, Satellite Orbit Number, Time of Acquisition, Perpendicular Baseline $B_\perp$, and Ocean Tidal Amplitude h_{tide} From the FES 2012 Tidal Model [*Carrère et al.*, 2012]

	Sensor	λ (cm)	Orbit	Date	$B_\perp$ (m)	h_{tide} (cm)
GL	ERS-1/ERS-2	5.6	24868	17 Apr 1996	−53.5	10.8
			5195	18 Apr 1996		2.2
			24367	13 Mar 1996	−185.8	−41.0
			4694	14 Mar 1996		−36.2
	CSK	3.125	27683	7 Dec 2013	334.6	−43.2
			16737	10 Dec 2013		0.753
			32660	22 Dec 2013	58.8	−37.2
			16974	26 Dec 2013		−13.5
DEM	TDX	3.1	21	2 Jun 2013	94.4	
			112	30 Jun 2013	69.4	
			163a	22 Jun 2013	235.1	
			163b	5 Aug 2013	195.2	

were acquired simultaneously so that the radar signal is not contaminated by ice motion, the turbulent wet atmosphere, the ionosphere, or oceanic tides. We employ the satellite ephemeris data to calculate the interferometric baseline and adjust the absolute phase of the interferogram to get absolute surface elevation by minimizing the difference between the laser-derived OIB surface elevation and the inferred surface elevation. Multiple TDX tracks and orbits are employed to stack the results and reduce errors. Comparing the results with OIB laser elevation data, we estimate a root mean square error of the DEM of 3 m (Figure S4). The residual error is caused by (1) the uncertainty in OIB laser elevation (10–30 cm in *Young et al.* [2015]), (2) changes in surface elevation between 2009 and 2012 (1–2 m), (3) unknown spatial variations in penetration depth in snow of the radar signals versus laser altimetry, and (4) changes in oceanic tides on the ice shelf. The resulting DEM (Figure 1a) has a 20 m spacing. We subtract the MC-derived ice thickness from the DEM converted into solid ice equivalent using a firn depth correction from RACMO2 [*Ligtenberg et al.*, 2011] to obtain the ice draft elevation in ice equivalent (Figure 1b).

Hydrostatic Potential Calculation. We use the TDX DEM and ice draft to calculate the hydrostatic potential (HP) of ice expressed in meters of elevation above hydrostatic equilibrium (Figure 1c) following *Shreve* [1972]. Surface elevations are referenced to mean sea level using the EIGEN-6C geoid [*Förste et al.*, 2012]. We assume a density of 917 kg/m^3 for ice and 1028 kg/m^3 for seawater since the ice shelf thickness calculated using these values assuming hydrostatic equilibrium best fits the OIB ice thickness data. We estimate the nominal error in HP to be 8 m from the 3 m nominal error in the DEM and 60 m error for the ice draft (scaled by 0.1).

Grounding Line Mapping. To detect the grounding line, we construct D-InSAR interferograms (DSI, Figure 2) using data acquired by the European Remote Sensing (ERS-1/ERS-2) radar satellite in 1996 and the Agenzia Spaziale Italiana (ASI) COSMO-SkyMed (CSK) constellation in 2013 (Table 1) following the approach in *Rignot et al.* [2011a]. Surface topography is removed from the DSI using the 20 m spacing TDX DEM. The two CSK interferograms are separated by 3 and 4 days, respectively. The 4 day interferogram is unwrapped and scaled to 3 days to be combined with the 3 day second interferogram. Good signal coherence is challenging to obtain in the TG area due to katabatic winds and high accumulation of snowfall [*Goodwin*, 1990]. CSK radar signals at X band (3.1 cm wavelength) are affected by this surface weathering. In addition, the shear margins of TG along Law Dome experience high strain rates, which generates phase aliasing and makes it difficult to unwrap the interferometric phase across the margins. The perpendicular baseline of the CSK DSI is 333 m, which corresponds to an altitude of ambiguity (or change in elevation causing a full phase cycle) of 26 m. In order to retrieve the ice vertical motion associated with tidal motion, it is therefore critical to remove the surface topography signal from a high-quality, high-resolution DEM. The BEDMAP 2 topography [*Fretwell et al.*, 2013] is not of sufficient quality for this exercise (Figure S6), while the TDX DEM yields only small residual motion signals.

Due to limited CSK data acquisitions in the TG sector, our mapping of grounding line is limited to 20% of the entire grounding zone of TG (Figure 2b). This portion of the grounding line, however, carries 70% of the

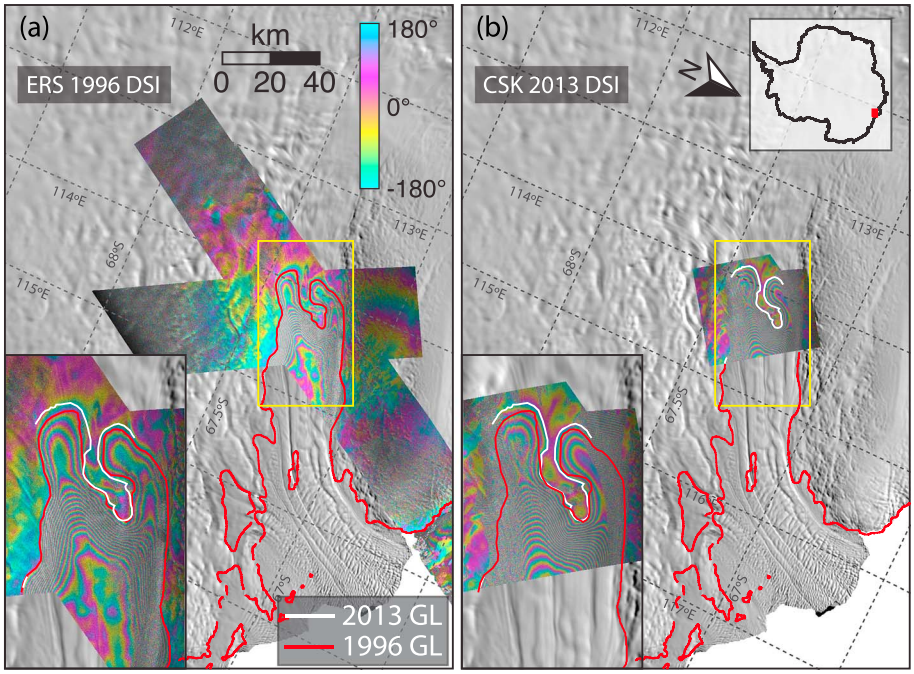

Figure 2. Differential SAR interferograms (DSIs) of Totten Glacier, East Antarctica, from (a) 1996 ERS-1/ERS-2 and (b) 2013 COSMO-Skymed (CSK) data overlaid on a MODIS mosaic of Antarctica [*Scambos et al.*, 2007]. The fringe pattern is caused by vertical tidal motion between data acquisitions. Grounding line in 1996 is red, and 2013 is white. Each fringe color coded from blue to yellow, purple, and blue again is a full cycle in interferometric phase or 360°.

total ice discharge into the ocean and coincides with the area of most rapid thinning reported by altimeters (see Figure 8 supporting information in *Pritchard et al.* [2009]). This area is therefore the key to monitor glacier changes.

A second DSI is formed using ERS-1/ERS-2 1996 data [*Rignot*, 2002] reprocessed using a longer track with the following improvements (Figure 2a): (1) the precision baseline is calculated using OIB laser altimetry data instead of BEDMAP 1 [*Lythe et al.*, 2001], (2) surface topography is removed using the TDX DEM, and (3) we apply a small correction (0.5%) of the line-of-sight ice velocity to remove phase residuals caused by subtle changes in ice motion during the 35 day period between consecutive ERS-1/ERS-2 pairs. Accurate baseline information and ice motion correction improve the quality of the DSI; i.e., data noise is reduced, and the transition boundary between floating and grounded ice is more easily detected. To map the grounding line, we multiply the phase signal by a factor of 4 to enhance the transition boundary, follow isocontours of tidal-induced displacements, and quantify the error in grounding line position across the glacier width. On average, the mapping precision is 1–2 pixels in the CSK DSI and 2–3 pixels in the ERS-1/ERS-2 DSI, which translates into a grounding line mapping error of less than 120 m.

To compare the grounding line position with tidal forcing, we use the Finite Element Solution (FES) 2012 global tidal model [*Carrère et al.*, 2012] to simulate the geocentric tidal heights at the time of acquisition of each SAR scene (Table 1). The model simulation is carried out at 66.5°S, 117°E. The calculated tidal amplitudes vary from −64 cm to 82 cm. We adopt a hydrostatic balance relationship from *Park et al.* [2013] and *Tsai and Gudmundsson* [2015] to quantify the grounding line migration associated with both oceanic tides and ice thinning:

$$\dot{h} - \left(\frac{\rho_{sw}}{\rho_i}\right)\dot{z} = \begin{cases} \left[\alpha - \beta\left(1 - \frac{\rho_{sw}}{\rho_i}\right)\right]\dot{x}, & \text{if } \dot{x} < 0 \\ \left[\left(\frac{\rho_i}{\rho_{sw}-\rho_i}\right)\alpha - \beta\right]\dot{x}, & \text{if } \dot{x} > 0 \end{cases} \quad (1)$$

where $\dot{z}$ is the change in tidal amplitude, $\dot{x}$ is the grounding line migration rate, $\dot{h}$ is the change in ice thickness, and α and β are the slopes of the ice surface and glacier bed, measured positive when elevation decreases

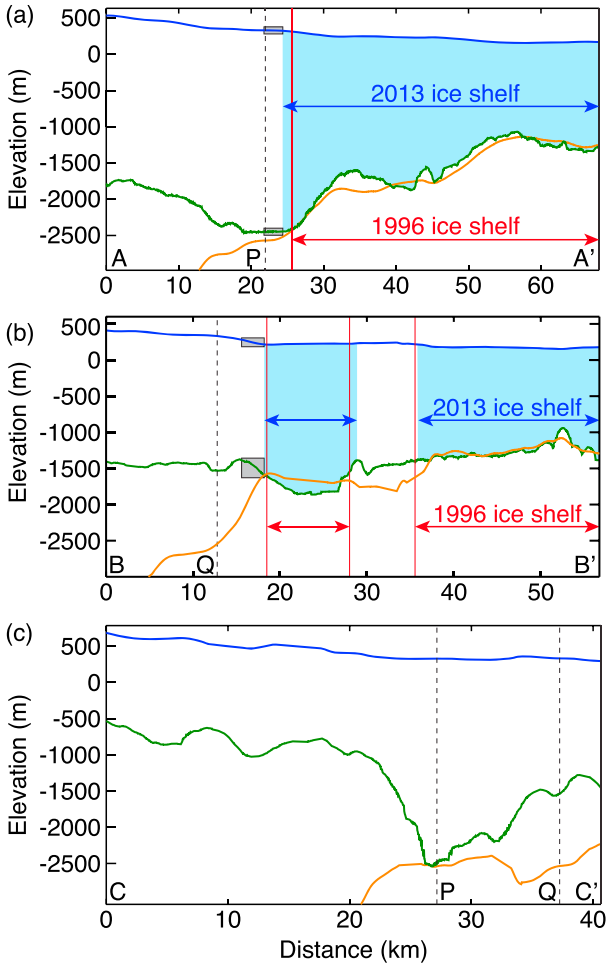

Figure 3. NASA Operation IceBridge (OIB) surface (blue), ice draft (green), and hydrostatic equilibrium ice bottom (orange) of Totten Glacier, East Antarctica, along tracks (a) AA′, (b) BB′, and (c) CC′ in Figure 1a. Blue shade is floating ice based on the 2013 grounding line mapping. Ice floatation in 1996 is delineated by a red line. P and Q mark the intersections of AA′ and BB′ with CC′, respectively. Grey boxes in Figures 3a and 3b delineate the portion over which we calculate surface and bed slopes.

down glacier. During the time interval of the ERS-1/ERS-2 and CSK data, we calculate a maximum grounding line migration of 200 m along the southern lobe and 50 m along the northern lobe, which is 4 to 12 times less than the grounding line migration measured between 1996 and 2013. Ice thinning over one tidal cycle is negligible.

3. Results

The grounding line of TG exhibits a complex and unusual pattern with two lobes extending more than 15 km inland across the 25 km glacier width of the fast-flowing core of TG (Figure 2) [*Rignot et al.*, 2011a]. The comparison between 1996 and 2013 reveals a widespread retreat of the grounding line of up to 3 km. The retreat is not uniform. The southern lobe retreated 1.1–2.6 ± 0.1 km, while the northern lobe retreated 0.4–1.3 ± 0.1 km. These values are significantly larger than those expected from changes in oceanic tides mentioned earlier, therefore indicative of a significant change. We also note that the shape of the grounding line changed. The two lobes are wider and more closely spaced in 2013 than in 1996 (Figure 2). The grounded region or ice island in between the two lobes decreased in area between 1996 and 2013, hence is thinning and ungrounding.

The tidal displacement measured from the DSIs is +0.46 m for ERS-1/ERS-2 1996 DSI and −0.40 m for CSK 2013 DSI. When comparing these values with the tidal predictions from FES 2012 (see Table 1), we find that FES 2012 correctly predicts the sign of the tidal motion but underestimates its amplitude by a factor of 2. This may be due to uncertainties in the shape of the sub-ice shelf cavity in the tidal model. If we assume that both the phase and magnitude of the FES 2012 are correct, we calculate using equation (1) that the grounding line retreat is underestimated by 30 m due to higher tidal uplift in the 1996 DSI compared to the 2013 DSI. The maximum grounding line migration due to tides is 60 m if we multiply the FES 2012 tidal magnitudes by a factor of 2 to match the observations.

The reconstructed MC ice draft reveals a fjord-like landscape with a deep trough spanning the entire 25 km width of the fast portion of TG (Figure 1b). The trough is 2000–2300 m deep and bounded by 2000 m high walls on both sides. The bed topography immediately upstream the two lobes is different: the southern lobe is 500 m deeper than the northern lobe. Upstream of the southern lobe, the bed remains nearly level at the center (slope of −0.3%, 17–24 km on OIB track AA′, Figure 3a) for another 7 km, then rises slowly with a 4% slope (0–17 km on AA′, Figure 3a). In contrast, the northern lobe sits on a prograde bed; i.e., the bed rises upstream of the grounding line with a 7.5% slope for 3 km (15–18 km on OIB track BB′, Figure 3b) and then flattens out (0–15 km on BB′, Figure 3b). The selected OIB lines AA′ and BB′ run through the center of the lobes, approximately parallel to the ice flow.

The bed topography is strongly reflected in the HP map (Figure 1c). In the proximity of the grounding line, the hydrostatic potential is mostly in the range of 0–20 m. Upstream of the southern lobe, we detect a 7 km long by 8 km wide "ice plain," similar to the one reported for Pine Island Glacier [*Corr et al.*, 2001], i.e., an area with relatively flat surface topography, grounded only a few tens of meters above hydrostatic equilibrium (see inset of Figure 1c, between 2013 CSK grounding line and 50 m HP contour). Beyond the northern lobe, the HP contours are more closely spaced. The ice island separating the two lobes is less than 60 m above hydrostatic equilibrium, hence apparent to an ice rumple, i.e., an area where ice overrides a bump in the seafloor but does not decrease its speed to zero.

Figure 3 shows the ice surface elevation and ice draft elevation along OIB tracks AA′, BB′, and CC′ and the departure of the ice draft from hydrostatic equilibrium. Along AA′ on the southern lobe, the ice draft shows no significant deviation from hydrostatic equilibrium ($<$ 120 m) until 7 km upstream of the grounding line, which marks the virtual limit of the ice plain. Along BB′, the ice draft rises and diverges from the hydrostatic equilibrium immediately upstream of the grounding line: the hydrostatic ice bottom drops by 500 m in 2 km while moving inland. At the location of the ice island separating the two lobes, we find no bedrock ridge, but we note the presence of a 50 m bump in surface elevation (see also Figure 1a). CC′ is a transverse flight track located 2 km upstream of the 2013 grounding line. CC′ intersects AA′ and BB′ at locations P and Q, respectively, which are upstream of the southern and northern lobes (Figure 1a). At P, the ice is close to hydrostatic equilibrium and grounded 2400 m below sea level. At Q, the ice draft is only 1400 m deep, and the ice is well above hydrostatic equilibrium.

Using equation (1), we calculate the thinning rate along each lobe that would explain the observed grounding line retreat in 1996–2013. We find that the ice thinning must average 0.7 m/yr in order to match the observed retreat. One percent error in the slope calculation using OIB data and ~10% error in the grounding line retreat together contribute to up to 12.5% error, or 0.09 m/yr, in the thinning result. This 0.7 ± 0.09 m thinning magnitude is consistent with the values reported in Table S1 for the same time period.

We use equation (1) to project future grounding line retreat if ice thinning persists at 0.7 m/yr. We estimate the glacier surface and bed slopes at the grounding line and apply equation (1) to calculate the retreat rate (see supporting information). The retreat rate is largest (480–720 m per 1 m ice thinning) along the southern lobe due to its low-HP gradient, and decreases to 20–70 m per 1 m thinning along the northern lobe due to its steeper topography. The retreat rate decreases to less than 1 m per 1 m ice thinning toward the sides. The projected grounding line caused by a 10 m ice thinning (0.7 m/yr in 14 years) is shown in Figure 1c. As the grounding line retreats, the southern lobe starts to float first. The grounded region in between the two lobes shrinks dramatically to become an isolated pinning point.

For verification, we repeat the same calculation along OIB profiles AA′ and BB′ (grey boxes in Figure 3) where high resolution, direct observational data are available. The retreat rates along AA′ and BB′ are 680 m and 27 m per 1 m ice thinning, respectively, which falls in the range of those calculated using the MC and TDX topographies. We note that this retreat rate is larger than that observed between 1996 and 2013; i.e., the region upstream of the 2013 grounding line is more prone to ungrounding than the region that ungrounded in 1996–2013. If thinning persists, we therefore project a faster retreat of the grounding line in years to come.

4. Discussion

Our analysis of the 1996 and 2013 radar data indicates that the grounding line of TG is complex and comprises two prominent lobes grounded only a few 10 m above hydrostatic equilibrium that extend 15 km inland. The pattern of grounding line retreat is asymmetrical. The retreat is 3 times larger on the southern lobe than on the northern lobe. The high-resolution maps of the ice surface and ice draft indicate that this pattern of retreat is consistent with the HP of the ice if we assume that ice has been thinning at an average rate of 0.7 m/yr between 1996 and 2013 or a total of 12 m between 1996 and 2013. The northern lobe has a bed topography that rises slowly inland, which favors slow retreat for a given amount of thinning, compared to the southern lobe which has a nearly flat bed and favors rapid retreat. Upstream of the southern lobe, there is a 7 km long region where ice is only grounded a few tens of meters above hydrostatic equilibrium with nearly flat surface and bed slopes, which we refer to as an ice plain. The ice plain region is prone to rapid retreat, as in the case of Pine Island Glacier, West Antarctica [*Corr et al.*, 2001]. Upstream of that region, however, the bed rises again and, the retreat would slow down significantly for the same amount of thinning.

If ice thinning rates were to maintain in the coming years, the rate of retreat would increase along the southern lobe. The ice plain region of TG may unground with only a modest amount of ice thinning. The ungrounding of TG would reduce basal resistance to ice flow, which would increase the glacier speed; increase the rate of ice thinning due to longitudinal stretching of the ice; and in turn accelerate the rate of grounding line retreat. This positive feedback has been observed on Pine Island Glacier, West Antarctica, during the rapid ungrounding of its ice plain in 2004–2009 [*Rignot et al.*, 2014]. A detailed numerical modeling of the ice flow of TG will be required to quantify the exact amount of speed up associated with further retreat.

The trough at the grounding line of TG is 2300 m below sea level and connects with the Vanderford Subglacial Trench around Law Dome (Figure 1b, top right). However, we do not find channels that would dissect the bed topography upstream of the grounding line to create favorable pathways for rapid retreat. Toward the southwest, the bed rises upstream of the 2013 grounding line along the northern lobe and past the ice plain for the south lobe, until 40 km further inland. This means that the main trunk of TG will not be retreating on a retrograde bed and be prone to a marine instability in the coming years.

A recent study [*Greenbaum et al.*, 2015] indicated possible ocean access to TG on the broad eastern side of its grounding line (Point F on Figure 1a). While it would be of interest to map grounding line retreat in that sector, the satellite data needed for this work do not exist.

The ongoing grounding line retreat of TG, about $1-3 \pm 0.1$ km in 17 years, is 1 order magnitude smaller than that observed in the Amundsen Sea sector of West Antarctica, at around 1–2 km/yr [*Rignot et al.*, 2014], and we find no retrograde channels in the immediate vicinity of the grounding line of TG that would accelerate the rate of grounding line retreat. Yet TG hosts 4 times the sea level equivalent of the Amundsen Sea sector so that any amount of grounding retreat of TG may still bare significant consequences for sea level rise from Antarctica. It is critical to continue and improve the monitoring of this region. Remote sensing of TG is challenging because the basin has few reference points for velocity mapping [*Mouginot et al.*, 2012], and coherence of the radar signals is hard to maintain due to surface weathering and high snowfall near Law Dome. To the best of our knowledge, it is the first time that the grounding line migration of TG has been mapped. At present, no other data exist to study its grounding line dynamics. In the future, the mapping may be extended using ALOS PALSAR-2 14 day repeat data or European Sentinel 1a's data on a 12 day repeat cycle.

5. Conclusions

A detailed mapping of the grounding line region of Totten Glacier, East Antarctica, reveals a 1500–2300 m deep grounding zone at the glacier center that extends 15 km inland along two side lobes grounded only 15–50 m above hydrostatic equilibrium, or ice plain. By comparing InSAR data acquired 17 years apart, we detect a $1-3 \pm 0.1$ km retreat of the grounding line. The retreat is asymmetrical along the two-lobe pattern but consistently indicates ice thinning of 12 m in 17 years or 0.7 m/yr at the grounding line on average. Over the same time period, a large fraction of the ice shelf has been observed to thin and thicken for a total net change not significantly different from zero [*Paolo et al.*, 2015]. More work is needed to elucidate the causes of the changes. If ice thinning continues, we project further grounding line retreat for another 7 km, after which rising bed elevation will slow down the retreat and protect it from a marine instability. Despite this configuration, it remains critical to obtain additional observations of this large marine-based sector to understand its evolution.

Acknowledgments

This work was performed at the University of California Irvine and at the California Institute of Technology's Jet Propulsion Laboratory, under contract NNX13AN46G, NNX14AN03G, and NNX14AB93G with the Cryosphere Science Program of National Aeronautics and Space Administration. ERS-1/ERS-2 TanDEM data were provided by European Space Agency. TanDEM-X data were provided by German Aerospace Center (DLR), through project XTI_GLAX0343. COSMO-SkyMed data ©ASI (2013) were provided by e-GEOS under ESA's TPM scheme (category 1 proposal ID 14871). We thank Dana Floricioiu from DLR for her advice on TanDEM-X processing.

The Editor thanks two anonymous reviewers for their assistance in evaluating this paper.

References

Bamber, J. L., R. E. M. Riva, B. L. Vermeersen, and A. M. LeBrocq (2009), Reassessment of the potential sea-level rise from a collapse of the West Antarctic Ice Sheet, *Science*, *324*(5929), 901–903.

Bindoff, N. L., M. A. Rosenberg, and M. J. Warner (2000), On the circulation and water masses over the Antarctic continental slope and rise between 80 and 150°E, *Deep Sea Res. Part II*, *47*(12-13), 2299–2326.

Blankenship, D. D., S. D. Kempf, and D. A. Young (2011, updated 2013), IceBridge HiCARS 1/2 L2 geolocated ice thickness 2009–2012, NASA DAAC at the NSIDC.

Carrère, L., F. Lyard, M. Cancet, A. Guillot, and L. Roblou (2012), FES 2012: A new global tidal model taking advantage of nearly 20 years of altimetry, *Proceedings of 20 years of Altimetry, Venice 2012*.

Chen, J. L., C. R. Wilson, D. D. Blankenship, and B. D. Tapley (2009), Accelerated Antarctic ice loss from satellite gravity measurements, *Nat. Geosci.*, *2*(12), 859–862.

Corr, H. F. J., C. S. M. Doake, A. Jenkins, and D. G. Vaughan (2001), Investigations of an "ice plain" in the mouth of Pine Island Glacier, Antarctica, *J. Glaciol.*, *47*(156), 51–57.

Flament, T., and F. Rémy (2012), Dynamic thinning of Antarctic glaciers from along-track repeat radar altimetry, *J. Glaciol.*, *58*(211), 830–840.

Förste, C., et al. (2012), A preliminary update of the direct approach GOCE processing and a new release of EIGEN-6C, *AGU Fall Meeting Abstracts*.

Fretwell, P., et al. (2013), Bedmap2: Improved ice bed, surface and thickness datasets for Antarctica, *The Cryosphere*, *7*, 375–393.
Goodwin, I. D. (1990), Snow accumulation and surface topography in the katabatic zone of Eastern Wilkes Land, Antarctica, *Antarct. Sci.*, *2*(3), 235–242.
Greenbaum, J. S., et al. (2015), Ocean access to a cavity beneath Totten Glacier in East Antarctica, *Nat. Geosci.*, *8*, 294–298.
Gwyther, D. E., B. K. Galton-Fenzi, J. R. Hunter, and J. L. Roberts (2014), Simulated melt rates for the Totten and Dalton ice shelves, *Ocean Sci.*, *10*, 267–279.
Horwath, M., B. Legrésy, F. Rémy, F. Blarel, and J. -M. Lemoine (2012), Consistent patterns of Antarctic ice sheet interannual variations from ENVISAT radar altimetry and GRACE satellite gravimetry, *Geophys. J. Int.*, *189*, 863–876.
Khazendar, A., M. P. Schodlok, I. Fenty, S. R. M. Ligtenberg, E. Rignot, and M. R. van den Broeke (2013), Observed thinning of Totten Glacier is linked to coastal polynya variability, *Nat. Commun.*, *4*, 2857.
Lenaerts, J. T. M., and M. van den Broeke (2012), Modeling drifting snow in Antarctica with a regional climate model: 2. Results, *J. Geophys. Res.*, *117*, D05109, doi:10.1029/2010JD015419.
Ligtenberg, S. R. M., M. M. Helsen, and M. R. van den Broeke (2011), An improved semi-empirical model for the densification of Antarctic firn, *The Cryosphere*, *5*(2005), 809–819.
Lythe, M. B., D. G. Vaughan, and the BEDMAP Consortium (2001), BEDMAP: A new ice thickness and subglacial topographic model of Antarctica, *J. Geophys. Res.*, *106*(B6), 11,335–11,351.
McMillan, M., A. Shepherd, A. Sundal, K. Briggs, A. Muir, A. Ridout, A. Hogg, and D. Wingham (2014), Increased ice losses from Antarctica detected by CryoSat-2, *Geophys. Res. Lett.*, *41*, 3899–3905, doi:10.1002/2014GL060111.
Morlighem, M., E. Rignot, H. Seroussi, E. Larour, H. Ben Dhia, and D. Aubry (2011), A mass conservation approach for mapping glacier ice thickness, *Geophys. Res. Lett.*, *38*, L19503, doi:10.1029/2011GL048659.
Mouginot, J., B. Scheuchl, E. Rignot, and R. Data (2012), Mapping of ice motion in Antarctica using synthetic-aperture radar data, *Remote Sens.*, *4*(9), 2753–2767.
Paolo, F. S., H. A. Fricker, and L. Padman (2015), Volume loss from Antarctic ice shelves is accelerating, *Science*, *348*(6232), 327–332.
Park, J. W., N. Gourmelen, A. Shepherd, S. W. Kim, D. G. Vaughan, and D. J. Wingham (2013), Sustained retreat of the Pine Island Glacier, *Geophys. Res. Lett.*, *40*, 2137–2142, doi:10.1002/grl.50379.
Pollard, D., R. M. Deconto, and R. B. Alley (2015), Potential Antarctic Ice Sheet retreat driven by hydrofracturing and ice cliff failure, *Earth Planet. Sci. Lett.*, *412*, 112–121.
Pritchard, H. D., R. J. Arthern, D. G. Vaughan, and L. A. Edwards (2009), Extensive dynamic thinning on the margins of the Greenland and Antarctic ice sheets, *Nature*, *461*(7266), 971–975.
Pritchard, H. D., S. R. M. Ligtenberg, H. A. Fricker, D. G. Vaughan, M. R. van den Broeke, and L. Padman (2012), Antarctic ice-sheet loss driven by basal melting of ice shelves, *Nature*, *484*(7395), 502–505.
Rignot, E. (2002), Mass balance of East Antarctic glaciers and ice shelves from satellite data, *Ann. Glaciol.*, *34*, 217–227.
Rignot, E. (2006), Changes in ice dynamics and mass balance of the Antarctic ice sheet, *Philos. Trans. R. Soc. London, Ser. A*, *364*, 1637–1655.
Rignot, E. (2008), Changes in West Antarctic ice stream dynamics observed with ALOS PALSAR data, *Geophys. Res. Lett.*, *35*, L12505, doi:10.1029/2008GL033365.
Rignot, E., and R. H. Thomas (2002), Mass balance of polar ice sheets, *Science*, *297*(5586), 1502–1506.
Rignot, E., J. Mouginot, and B. Scheuchl (2011a), Antarctic grounding line mapping from differential satellite radar interferometry, *Geophys. Res. Lett.*, *38*, L10504, doi:10.1029/2011GL047109.
Rignot, E., J. Mouginot, and B. Scheuchl (2011b), Ice flow of the Antarctic ice sheet, *Science*, *333*(6048), 1427–1430.
Rignot, E., S. Jacobs, J. Mouginot, and B. Scheuchl (2013), Ice shelf melting around Antarctica, *Science*, *341*(6143), 266–270.
Rignot, E., J. Mouginot, M. Morlighem, H. Seroussi, and B. Scheuchl (2014), Widespread, rapid grounding line retreat of Pine Island, Thwaites, Smith, and Kohler glaciers, West Antarctica, *Geophys. Res. Lett.*, *41*, 3502–3509, doi:10.1002/2014GL060140.
Scambos, T., T. M. Haran, M. Fahnestock, T. H. Painter, and J. Bohlander (2007), MODIS-based Mosaic of Antarctica (MOA) data sets: Continent-wide surface morphology and snow grain size, *Remote Sens. Environ.*, *111*(2-3), 242–257.
Shepherd, A., and D. Wingham (2007), Recent sea-level contributions of the Antarctic and Greenland ice sheets, *Science*, *315*(5818), 1529–1532.
Shreve, R. L. (1972), Movement of water in glaciers, *J. Glaciol.*, *11*, 205–214.
Spence, P., S. M. Griffies, M. H. England, A. M. Hogg, O. A. Saenko, and N. C. Jourdain (2014), Rapid subsurface warming and circulation changes of Antarctic coastal waters by poleward shifting winds, *Geophys. Res. Lett.*, *41*, 4601–4610, doi:10.1002/2014GL060613.
Sun, S., S. L. Cornford, Y. Liu, and J. C. Moore (2014), Dynamic response of Antarctic ice shelves to bedrock uncertainty, *The Cryosphere*, *8*, 1561–1576.
Tsai, V. C., and G. H. Gudmundsson (2015), An improved model for tidally-modulated grounding-line migration, *J. Glaciol.*, *61*(226), 216–222.
Velicogna, I., T. C. Sutterley, and M. R. van den Broeke (2014), Regional acceleration in ice mass loss from Greenland and Antarctica using GRACE time-variable gravity data, *J. Geophys. Res. Space Physics*, *119*, 8130–8137, doi:10.1002/2014GL061052.
Weertman, J. (1974), Stability of the junction of an ice sheet and an ice shelf, *J. Glaciol.*, *13*(67), 3–11.
Williams, G., A. J. S. Meijers, A. Poole, P. Mathiot, T. Tamura, and A. Klocker (2011), Late winter oceanography off the Sabrina and BANZARE coast (117128E), East Antarctica, *Deep Sea Res. Part II*, *58*(9-10), 1194–1210.
Wright, A. P., et al. (2012), Evidence of a hydrological connection between the ice divide and ice sheet margin in the Aurora Subglacial Basin, East Antarctica, *J. Geophys. Res.*, *117*, F01033, doi:10.1029/2011JF002066.
Young, D. A., et al. (2011), A dynamic early East Antarctic Ice Sheet suggested by ice-covered fjord landscapes, *Nature*, *474*(7349), 72–75.
Young, D. A., et al. (2015), Instruments and methods: Land-ice elevation changes from photon-counting swath altimetry: First applications over the Antarctic ice sheet, *J. Glaciol.*, *61*(225), 17–28.
Zwally, J., M. B. Giovinetto, J. Li, H. G. Cornejo, M. A. Beckley, A. C. Brenner, J. L. Saba, and D. Yi (2005), Mass changes of the Greenland and Antarctic ice sheets and shelves and contributions to sea-level rise: 1992–2002, *J. Glaciol.*, *51*(175), 509–527.